Physics of Plasmas

Introducing adaptive cold atmospheric plasma: The perspective of adaptive cold plasma cancer treatments based on real-time electrochemical impedance spectroscopy

Cite as: Phys. Plasmas 27, 063501 (2020); https://doi.org/10.1063/5.0003528
Submitted: 02 February 2020 . Accepted: 06 May 2020 . Published Online: 01 June 2020

Li Lin, Zichao Hou, Xiaoliang Yao, Yi Liu, Jagadishwar R. Sirigiri, Taeyoung Lee, and Michael Keidar

Physics of Plasmas ARTICLE scitation.org/journal/php

Introducing adaptive cold atmospheric plasma: The perspective of adaptive cold plasma cancer treatments based on real-time electrochemical impedance spectroscopy

Cite as: Phys. Plasmas **27**, 063501 (2020); doi: 10.1063/5.0003528
Submitted: 2 February 2020 · Accepted: 6 May 2020 ·
Published Online: 1 June 2020

Li Lin,[1,a)] Zichao Hou,[1] Xiaoliang Yao,[1] Yi Liu,[1,2] Jagadishwar R. Sirigiri,[3] Taeyoung Lee,[1] and Michael Keidar[1]

AFFILIATIONS

[1]Department of Mechanical and Aerospace Engineering, The George Washington University, 800 22nd St., NW, Washington, DC 20052, USA
[2]School of Energy and Power Engineering, Nanjing University of Science and Technology, 200 Xiaolingwei St., Nanjing 210094, People's Republic of China
[3]Bridge 12 Technologies, Inc., 37 Loring Dr., Framingham, Massachusetts 01702, USA

[a)]**Author to whom correspondence should be addressed**: lilin@gwu.edu

ABSTRACT

Following the understanding of the cold atmospheric plasma jet control, the optimization of plasma parameters for biomedical applications has become an important area of research in the field of plasma-based cancer treatment. A real-time feedback signal is usually required by a control algorithm, such as a self-adaptive plasma jet, which is designed to automatically self-optimize its parameters to adapt to a variety of biomedical applications and situations. In this paper, we introduce the potential of replacing the cell viability or cell stress assay with electrochemical impedance spectroscopy (EIS) to provide a real-time feedback signal for a model predictive control (MPC) method aided by machine learning. The EIS frequency is in the kHz to GHz regime. Therefore, the MPC method is not only designed for minimizing the cancer cell viability, but also considered to optimize cell membrane behaviors and other chemical species dialing. Since these signals are in the range of GHz, we introduce alternatives for the impedance analyzer to measure the impedance spectrum, including a Fabry–Pérot resonator and one of its scanning-array variations.

I. SELF-ADAPTIVE COLD PLASMA CANCER TREATMENT

The medical use of plasma has been studied for decades, including blood coagulation, bacterial decontamination, tissue removal, and the cancer treatment using a cold atmospheric plasma jet (CAPJ).[1–5] CAPJ is a nonequilibrium plasma in which ions and molecules are at room temperature while the electron temperature remains high.[6,7] The main advantage of such a plasma-based cancer treatment is selectivity, i.e., different types of cells/tissues react differently to CAPJ. Therefore, using the difference correctly may effectively damage more cancer cells than normal cells.[8,9] However, it is also obvious that the noble gas guided plasma interacting with cells/tissues in the air can be unstable due to the disturbance of the environment and can vary significantly with the target, which is a boundary condition to the plasma.[10–16] The cold plasma therapy provides a combination of reactive nitrogen and oxygen species (RNOS) and the electromagnetic waves from RF to UV; hence, an optimization of plasma parameters becomes a prerequisite for targeting cancer cells with a consistent efficiency among a large variety of patients. One solution of such an issue is a self-adaptive cold atmospheric plasma jet (SACAPJ), which includes a control circuit sampling the cell/tissue target for a feedback signal to optimize the CAPJ in real-time and eventually maximize the selectivity. The control algorithm enables the CAPJ to adapt to patients and the local environment automatically.[17–19]

To achieve such a level of optimization control, a database of how cell lines react to CAPJ is usually required. As a nascent research field, only a few preliminary research articles have been published, including a model predictive control (MPC) method[20] and some machine learning approaches.[21,22] As the first approach, an MPC study on the SACAPJ for treating U87MG human primary

glioblastoma (brain cancer) and MDA-MB-231 human breast adenocarcinoma (breast cancer) was reported in Ref. 20. The first step of MPC in SACAPJ is to design a net proliferation rate function $F(t, p)$ (with unknown constants to be determined) for the cancer cell population model $\dot{p} = pF(t, p)$, where t is the time after treatment and p is the cell viability.[20,23] The next step, also called "system identification," is to fit the function $F(t, p)$ with experimental data to determine those unknown constants. The fitting is achieved by minimizing an objective function $J = \sum_{i=1}^{n} \int_0^{t_{tot}} \|p_i - p_{model}\|^2 dt$, where t_{tot} is the total time of cell observation, p_i represents the cell viability in the ith experiment, and p_{model} is the viability computed from the cancer cell population model.[20] For multiple control parameters, each of them has its objective function, and the final objective function becomes a weighted summation.[20] The final step is thus to select the correct control parameter setups to meet the treatment requirement that maximizes the selectivity. However, to ensure that the MPC method can accurately achieve the treatment objective, one-step MPC–CAPJ treatment is not enough.[20] The CAPJ treatment must be applied periodically when each treatment setup was determined by the MPC algorithm considering the actual cell viability.[20] Unfortunately, for biomedical experiments, cell viability is usually measured using 3-(4,5-dimethylthiazol-2-yl)-2,5-diphenyltetrazolium bromide (MTT) assay.[18] The method takes a couple of hours to acquire a result and makes the sample unusable after adding the MTT solution. Therefore, for an actual MPC optimized SACAPJ, real-time measurement of cell viability without deteriorating the sample is required. Generally, no matter what algorithm is designed for the CAPJ, even for machine learning, a feedback signal is always a key to reach the self-adaptive optimization. Due to the biomedical applications of SACAPJ, real-time direct measurement of cell/tissue conditions should be the top priority to solve, and one solution that should be considered is a well-developed technology: electrochemical impedance spectroscopy (EIS).

The first study of electric properties in biological tissues was performed in 1780 when Galvani discovered bioelectricity in his famous frog's legs experiment.[24] After that, in the 19th century, more research was done on the relevance of the bioelectricity in muscle tissue and nerve. With the help of electrical technology advancement, in the 20th century, the impedance analysis of tissues was developed based on the study of dielectric properties for both low and high frequencies.[25–29] In the last two decades, research in bioelectrical impedance has become increasingly widespread to the extent that about 1600 papers in this area have been published from 1990 to 2003.[30] For the impedance analysis, there is now a mature technology named Electrochemistry Impedance Spectroscopy which is fully functional in both the research environment and clinical diagnostics. Using EIS, researchers can identify and observe the behavior of biological cells in bulk fluids, in addition to macromolecules such as DNA and enzymes.[31] Moreover, such an observation is real-time during a cell culture.[32]

Therefore, EIS makes it possible to provide the information of not only the cell viability, but also the ion cloud around cells, membrane behaviors, and even chemical compositions such as reactive species and proteins. Hence, EIS can be considered as a powerful real-time sampling tool to collect feedback signals from the biomedical target and optimize the plasma. In this paper, we focus on the high-impact potential of merging EIS with the SACAPJ control system to achieve an optimized plasma treatment hardware for both laboratory research and clinical use. Furthermore, we present a data-based dynamic model for the cancer cell response, as an alternative to a heuristic approach.[20] Utilizing this, we propose a Model Predictive Learning Control (MPLC) framework, where the dynamic model is adjusted online based on the real-time measurements through EIS. Compared with the results of MPC,[20] the proposed learning framework does not require multiple periodic treatments to achieve the treatment goal.

II. A STANDARD ELECTROCHEMICAL IMPEDANCE SPECTROSCOPY ROUTINE

A basic example design of the EIS-SACAPJ hardware is shown in Fig. 1. To measure the impedance, two electrodes are immersed in the media for the cell culture. An AC voltage is applied to these electrodes with the frequency usually swept from DC to a few GHz frequencies.[33] When changing such an excitation frequency, the complex impedance will be recorded and analyzed. Based on the relation

$$\varepsilon^{*-1} = -\omega\varepsilon_0 Z_{IM} + j\omega\varepsilon_0 Z_{REAL}, \quad (1)$$

the measured impedance will indicate the complex permittivity properties as a function of frequency, where ε^* is the complex permittivity that $\varepsilon^* = \varepsilon' + j\varepsilon''$, j is the imaginary unit, ω is the angular frequency, ε_0 is the permittivity of vacuum, Z_{IM} is the imaginary of the impedance measured, and Z_{REAL} is the real part of it. The frequency response of both impedance and permittivity can be analyzed using a Bode plot, which shows both the magnitude and phase and in the Nyquist plot, which shows results in a complex plane.[33,34]

After the measurement, an equivalent circuit is formulated to fit the impedance results. The equivalent circuit is a combination of resistors, capacitors, inductors, and other nonideal circuit elements[33] such as constant phase elements (CPEs). Nonideal circuit elements are used for fitting nonlinear slopes of the impedance in frequency responses while an ideal capacitor has an impedance $Z = (2\pi fC)^{-1}$, where f is the frequency and C is the capacitance. The CPE is a revised model of a capacitor with a phase irrelevant to the excitation frequency. The impedance of the CPE can be designed as follows:[33]

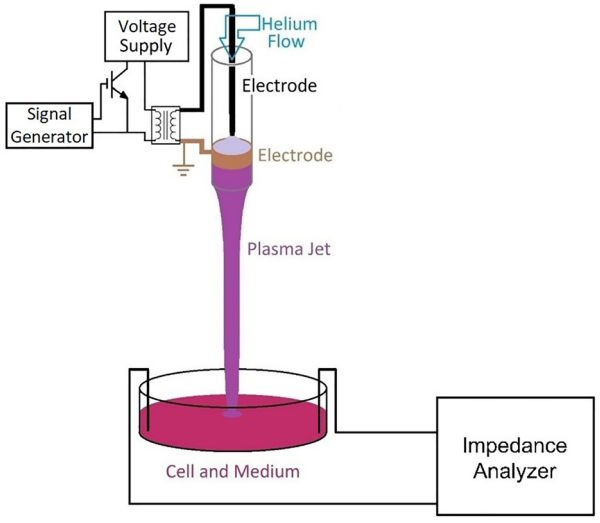

FIG. 1. A basic hardware setup of electrochemical impedance spectroscopy and self-adaptive cold atmospheric plasma jet.

$$Z_{CPE} = \frac{1}{Q\omega^{\alpha}}\left[\cos\left(\frac{\alpha\pi}{2}\right) - j\sin\left(\frac{\alpha\pi}{2}\right)\right], \tag{2}$$

where Q is known as the CPE in Ω^{-1} s^{α}, ω is the angular frequency of the excitation voltage, j is the imaginary unit, and α is the variable to make the CPE fit a nonlinear impedance. When $\alpha = 0$, the CPE can be considered as an ideal resistor. When $\alpha = 1$, the CPE is an ideal capacitor. Later in this work, the concept of CPEs will be used to describe the cell-media system such as the cell membrane and bulk media. Each of them will include their Q and α in the equivalent circuit. The combinations of these electrical elements simulate electrical behaviors and electrochemical processes of the species in the media. These events are summarized as follows:[33]

1. a "bulk media impedance" for species movements;
2. a double layer near an electrode has a "double layer capacitance";
3. charge transfer resistance;
4. species adsorption in double-layer cause an "electrochemical sorption impedance";
5. "mass transfer impedance" in double-layer.

Moreover, for an *in vitro* experiment, cells with the membrane and the plasma jet should also be considered. Therefore, the actual schematic of such an electrochemical-plasma-biomedical coupled problem can be summarized in Fig. 2.

First, for the bulk media, considered as an electrolyte, its impedance can be expressed as R_{bulk} paralleled with C_{bulk}. R_{bulk} represents the conductive part of the media which includes free ions, that

$$R_{bulk} = \frac{d_E}{A\sum z_i\mu_i C_i^*}, \tag{3}$$

where d_E is the distance between the electrodes, A is the interface area of the electrodes and media, and z_i, μ_i, and C_i^* are the charge, mobility, and concentration of the ith ion. C_{bulk} can be a CPE for a better result fitting, which is denoted as CPE_{bulk}. Similarly, the capacitance of the cell membrane is also defined as a CPE paralleled by an ideal resistor to represent the total cell impedance. These two elements will be denoted as CPE_{CMem} and R_{cell}.

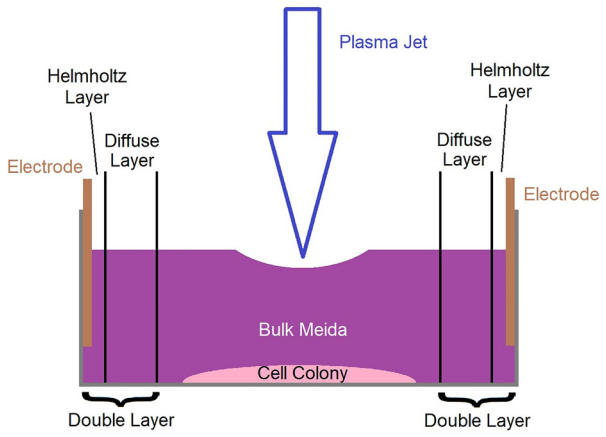

FIG. 2. The schematic diagram of plasma jet treatment and impedance spectroscopy.

Second, at the interface of the electrodes and bulk media, the electrolysis, species adsorption, desorption, and molecule polarization result in a special region named double layer, which consists of the Helmholtz layer and diffuse layer.[33] The capacitance of this region can be expressed as[33]

$$C_{DL}^{-1} = C_{Helmholtz}^{-1} + C_{diffuse}^{-1}, \tag{4}$$

$$C_{Helmholtz} = \varepsilon_r\varepsilon_0 L_H, \tag{5}$$

$$C_{diffuse} = \frac{\varepsilon_r\varepsilon_0}{\lambda_D}\cosh\left(\frac{z_i e\phi_D}{k_B T}\right), \tag{6}$$

where C_{DL}, $C_{Helmholtz}$, and $C_{diffuse}$ are the capacitance of double layer, Helmholtz layer, and diffuse layer. ε_r is the relative permittivity of the media, L_H is the thickness of Helmholtz layer which is usually 1–2 nm, e is the unit charge, ϕ_D is the potential between Helmholtz layer and diffuse layer, k_B is the Boltzmann constant, T is the local temperature, and the Debye length λ_D is the thickness of the diffuse layer, that[33]

$$\lambda_D = \sqrt{\frac{\varepsilon_r\varepsilon_0 k_B T}{8\pi e^2\sum z_i^2 C_i^*}}. \tag{7}$$

Similar to the plasma sheath, the potential changes contentiously across this layer.

In the process of electrolysis around the electrodes, an equilibrium potential of a redox reaction is established. When the electrode voltage differs from the equilibrium voltage, there will be a charge transfer that occurs at the interface. The resistance of charge transfer can be computed as[33]

$$R_{CT} = \frac{R_g T}{zFI_0}, \tag{8}$$

where R_g is the ideal gas constant, F is Faraday constant which equals to 96 500 C/mol, and I_0 is the charge transfer current that[33]

$$I_0 = zFAk_0 C_{OX}^{*1-\alpha} C_{RED}^{*\alpha}. \tag{9}$$

In this expression, C_{OX}^* and C_{RED}^* are the concentration of the oxidant and reductant in media, α is the reaction order, and k_0 is the kinetic rate constant of redox reaction that can be expressed using Eyring's equation[35]

$$k_0 = \frac{\alpha k_B T}{h}\exp\left(\frac{-\Delta G}{R_g T}\right), \tag{10}$$

where h is the Planck constant and ΔG is the Gibbs energy of activation in the redox reaction. The capacitance and resistance of the species adsorption at the interface can be computed as follows:[33]

$$C_{ads} = \frac{F^2 A\Gamma}{4RT}, \tag{11}$$

$$R_{ads} = \frac{2R_g T}{F^2 A\Gamma k_f}, \tag{12}$$

where Γ is the amount of adsorbed species in mol/cm^2 and k_f is the kinetic rate constant of adsorption which had been well defined.[36]

Also, mass transport occurs over the entire bulk of media especially in the double layer around the electrodes. This impedance is also named "Warburg impedance." Its value can be computed as

$$Z_W = \frac{R_g T(1-j)}{F^2 A \sum z_i^2 C_i^* \sqrt{2\omega D_i}}, \tag{13}$$

where D_i is the diffusion coefficient of the ith species. The coefficient value can be estimated by the Einstein–Smoluchowski relation that

$$D_i = \mu_i k_B T_i, \tag{14}$$

where μ_i and T_i are the mobility and temperature of the ith species.

With all the elements and processes defined above, the equivalent circuit can be designed as shown in Fig. 3 corresponding to the schematic diagram shown in Fig. 2. In this circuit, CPE_{bulk} and CPE_{CMem} are defined in Eq. (2), R_{bulk} and R_{cell} are defined in Eq. (3), C_{DL} is defined in Eq. (4), R_{CT} is defined in Eq. (8), C_{ads} is defined in Eq. (11), R_{ads} is defined in Eq. (12), and Z_W is defined in Eq. (13). After assuming and adjusting the variables in these equations, the frequency response of the equivalent circuit will fit the measured curves of impedance and permittivity.

A common result of permittivity for biological tissue had been shown in EIS publications.[37] The total permittivity drops in three stair-like patterns, which are named α, β, and γ dispersions. All of them are related to the electric properties of the cell membrane. The α dispersion is located in the Hz–kHz region. The low frequency corresponds to a long relaxation period. Based on the previous research,[37] three possible events of the cell membrane (or the combination of them) may lead to the α dispersion. First, the ion exchange through the membrane holes makes the membrane impedance as a function of frequency with a relaxation time of α dispersion. Second, the ion cloud around the cell causes the α dispersion of membrane conductivity. Third, the membrane itself may have a frequency response of both the α and β dispersion which is in the region of radio frequency. For the cells in suspensions, their properties of membrane can be computed using Maxwell–Wagner relaxation theory.[37] For the γ dispersion, the frequency is higher than 10 GHz. The inner substance of cells such as protein and water results in such a dispersion.[37] Moreover, some recent publications indicate that the electromagnetic emission from the CAPJ may enable the cells into an activation state that is more sensitive to reactive species and medicine.[38,39] One of the physical explanations of such a phenomenon is the membrane vibration due to the charges on the membrane oscillating in the incoming electromagnetic emission.[40–42] The membrane vibration thus produces an acoustic wave propagating through the intracellular substance. Such a theory may be verified using the EIS α dispersion for the membrane vibration and γ dispersion for the intracellular acoustic wave. Also, these measurements can be a part of a future advance control loop, since cell activation also involves in the cell viability.[38,39] However, to measure the high frequency γ dispersion, a more advanced technology should be considered instead of the impedance analyzer, which will be discussed later in this paper.

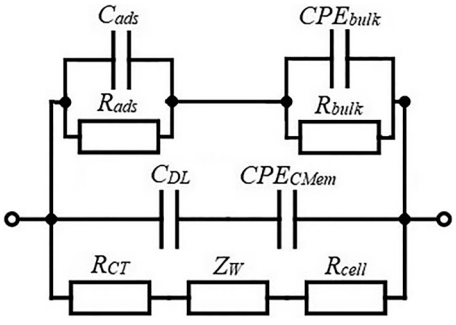

FIG. 3. An equivalent circuit of the cell-media combination.

Therefore, when the cells and media are treated by the CAPJ, the frequency response of impedance and permittivity will change accordingly. To fit the updated signals, some of the equivalent circuit parameters have to be changed. When these two results agree, the modified parameters along with the permittivity dispersion will provide the information to estimate the electrochemical process behind this signal shift. Note that, during the interaction with CAPJ, different patterns of the α and β dispersion should be expected, due to the kHz discharge frequency of CAPJ and the radio frequency of plasma oscillation.

III. PRELIMINARY IMPEDANCE SPECTROSCOPY IN MODEL PREDICTIVE CONTROL

Despite the standard procedure of EIS measurement introduced above, the equivalent circuit and analysis routine included in CAPJ optimization control can be simplified. This is due to the omittance of detailed species analysis in the media and the need to directly correlate the cell viability with the impedance spectrum as a feedback signal for the control loop.[20] Moreover, in such a case, the CAPJ treatment window is always between two neighbor EIS measurement periods. Therefore, such a setup can simplify the equivalent circuit that the Z_{CAPJ} at the top of the circuit can be removed.

A preliminary EIS measurement setup for the SACAPJ is shown in Fig. 4. An Agilent/HP 43961A RF impedance test kit with an HP 16092A fixture is used for the measurement. To avoid electrochemical contamination, the electrodes immersed in the media have to be noble metal. Two platinum (99.9% purity) pins are immersed in the media during the measurement with the other ends connected to the fixture. Figure 5 shows the resulting connection between the cell viability and the impedance spectrum of a CAPJ treating U87MG (brain tumor cancer cells) at a sinusoidal applied voltage of 8.4 kV pk–pk and the helium flow rate at 8.8 LPM. The detailed CAPJ schematic can be found in Fig. 1. Two significant peaks can be identified. One is located at around 300 MHz and the other one is at 549 MHz. For this example, we focus on the 549 MHz peak which is adequate for the

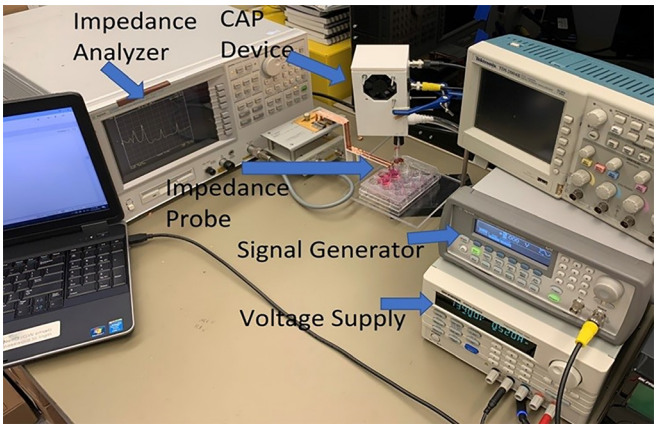

FIG. 4. Impedance measurement setup.

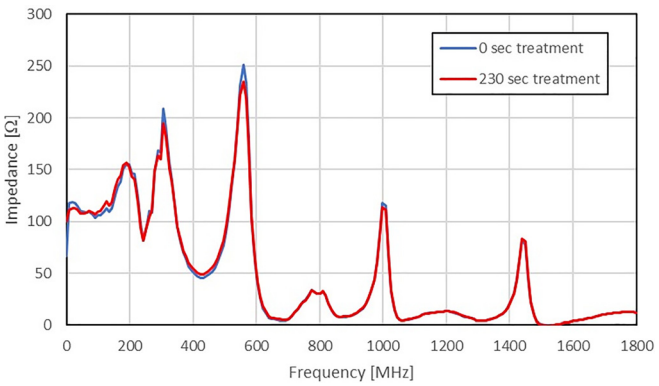

FIG. 5. Impedance spectrum of a plasma jet (8.4 kV) treatment on U87MG cells where the treatment times are shown in blue and red represent the impedance before and after the treatment.

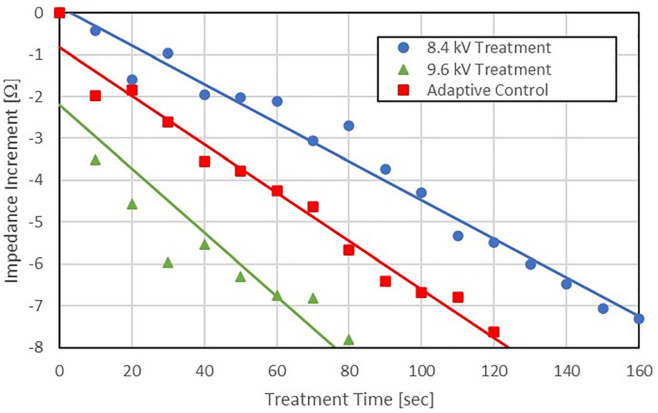

FIG. 7. The temporal evolution of the 549 MHz peak increments with applied voltage variation and an adaptive control trail.

demonstration. In Fig. 6, the peak increments at the end of treatment are compared with the cell viabilities. A linear decrement is revealed in this experiment that a lower impedance at 549 MHz implies lower U87MG viability. In addition, the EIS is measured at a higher applied voltage again, which is shown in Fig. 7. At 9.6 kV, the impedance decreases faster, which implies that the treatment time required for the same cell viability is shorter compared with the 8.4 kV case. Then, a simple adaptive trail is tested to control the impedance decrement speed by varying the applied voltage. The impedance at 549 MHz was measured every 10 s with the control of the impedance decrement speed. The desired impedance decrement speed value for this experiment is 0.6 Ω/10 s. The minimum and maximum applied voltages were set to 8.4 kV and 9. 8 kV. If the impedance decrement speed was higher than the desired value, the applied voltage would be lowered by 0.4 kV. If the impedance decrement speed was lower than the desired value, the applied voltage would be increased by 0.4 kV. Finally, the CAPJ was programmed to stop automatically after it reaches the impedance decrement point which was 7 Ω (it is about 40% of the normalized viability).

The proposed EIS is utilized in MPC to adjust the parameters to generate plasma, such as the plasma discharge voltage, treatment duration, or the flow rate, in accordance with the actual cancer response. The role of EIS is twofold: build data to construct a dynamic model of the cancer cell population prior to CAPJ treatments and real-time diagnostics to measure the actual cancer response *in situ*. The overall structure of EIS–MPC is illustrated in Fig. 8.

In addition to the conventional MPC presented in Ref. 20, here we present an MPLC framework, which focuses on learning aspects: the empirical model of cancer cell response presented in Ref. 20 is updated based on EIS measurements. The motivation is that it would be more desirable if the adaptive plasma system learns the dynamic characteristics of the particular cancer cell under treatment so that the mathematical model can be refined as the treatment is repeated. This provides a more accurate mathematical model that can be used to adjust the prospective treatment plan accordingly.

In particular, the cancer cell responses to several treatment conditions are modeled by a Gaussian Process (GP),[43] which is statistical modeling in machine learning that may account for the degree of confidence in the learned model. Suppose that we have a set of training data representing the cancer viability over time for various treatment conditions. GP provides a tool to generalize these data to predict the cancer viability at an arbitrary time instance for an arbitrary treatment condition. Figure 9 illustrates the GP prediction for an experimental result presented in Ref. 20, where the viability of U87MG is measured multiple times after it is treated with CAPJ. To have the consistent value of viability for several experiments, we normalize the cancer cell viability under Cold Atmospheric Plasma (CAP) treatments with the initial cancer cell viability just before the CAP exposure. The red curves in Fig. 9 present the corresponding mean and uncertainty

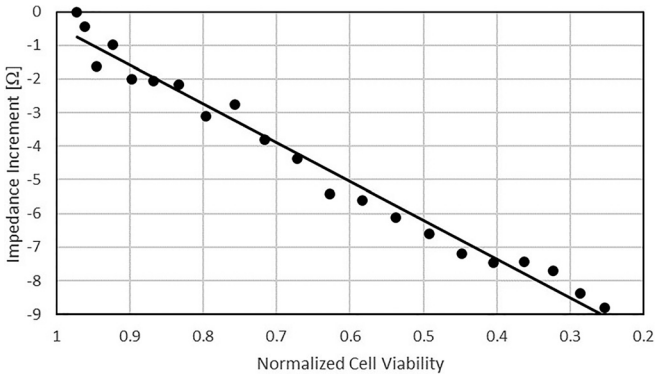

FIG. 6. The impedance increments at 549 MHz measured after a 0-230s treatment (8.4 kV applied voltage) corresponding to the cell viability measured 72 hours later.

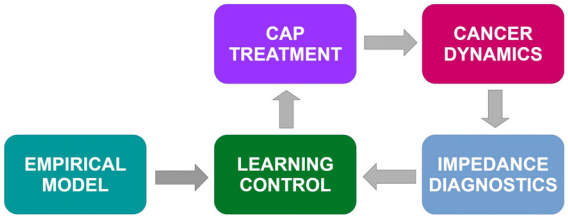

FIG. 8. MPLC framework.

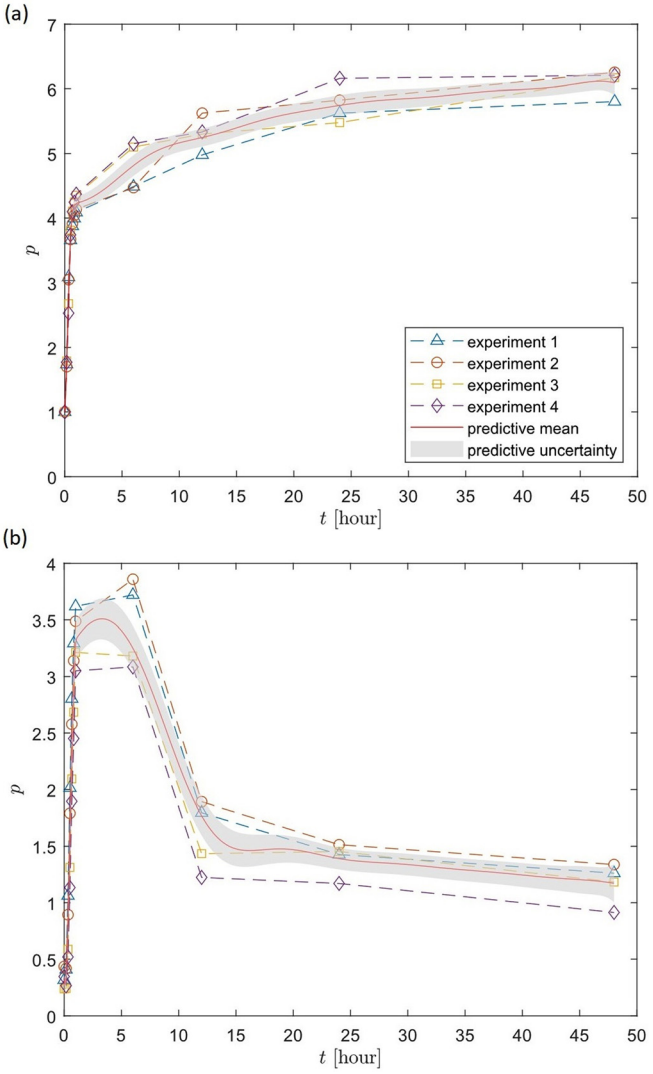

FIG. 9. Gaussian process regression results of U87MG for the applied voltage $U = 6.32$ kV with a treatment time of (a) 0 s and (b) 180 s.

predicted by GP with respect to the time after treatment for each of the two treatment durations. They are illustrated against four experimental data in Ref. 20. As shown in Fig. 9(a), the case without any CAP treatments has cancer cell viabilities boost up to 6, while in Fig. 9(b), the CAP treatment reduces such viabilities down to 1.5 with GP generalization.

Suppose that we are planning two consecutive CAPJ treatments to reduce the cancer viability up to a prescribed desired ratio. The first treatment can be determined based on the empirical model, i.e., we can select the treatment duration to reduce the cancer cell viability as desired. The actual cancer cell response to the first CAPJ may not be identical to the GP prediction, as the characteristics of cancer used to generate the empirical model might differ from cancer under treatments.

The EIS diagnostics provides cancer cell response for the particular cancer cells treated by CAPJ, which generates additional data that can be used to update the GP model. Then, the next treatment can be scheduled based on the GP model revised according to the actual response.

Figure 10 illustrates simulation results to reduce the cancer viability into 13% of the initial value through two CAP treatments over 48 h. The cell viability ratio defined in Fig. 10 is the ratio of normalized cell viability at any given time between the experimental group and control group that

$$r(t) = \frac{p_{experiment}(t)}{p_{control}(t)}, \quad t \in [0, 48]$$

where $p_{experiment}$ and $p_{control}$ are the data picked from one of our previous publication where many different cases are tested.[20] Specifically, the $p_{experiment}$ and $p_{control}$ of 180 s treatment time are shown in Figs. 9(b) and 9(a).

More specifically, the treatment objective for two treatments is illustrated by a red dashed curve, and the red solid curve corresponds to an ideal case of MPC where the predicted model is perfect. However, when there are errors in prediction, the actual response derives from it, as shown by the green curves. Finally, the proposed MPLC learns the dynamic characteristics of the actual cancer response after the first treatment, and the second treatment is determined by the learned model. Consequently, the cancer cell response after the second treatment, shown by black solid curves, closely resembles the ideal case.

This shows that the proposed MPLC achieves the treatment goal, while successfully compensating the discrepancy between the actual cancer response and the predicted response. This should be distinguished from the conventional MPC of Ref. 20, where the treatment objective is adjusted periodically based on the actual response without any learning. As such, it required multiple treatments to achieve the goal. Here, in the proposed MPLC, the learning process after the first treatment enables us to achieve the objective at the second treatment.

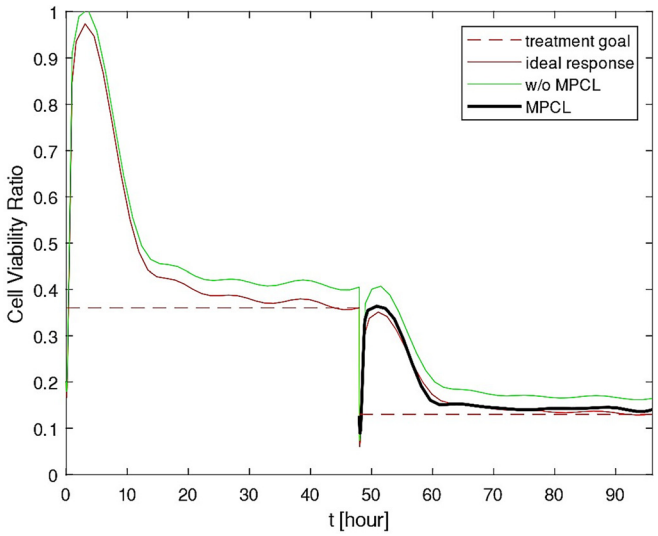

FIG. 10. Model predictive learning control for the plasma treatments of U87MG.

This approach utilizes all of the available data to tailor CAP particularly to the cancer cells under treatments. Furthermore, the stochastic Bayesian learning of GP gauges the level of confidence when fusing information, thereby providing safe and robust learning that is not erroneously disturbed by noisy data.

Generally, EIS-MPLC control can be more powerful than simply working with cell viability. The spectrum in Fig. 4 is merely a part of β dispersion introduced in Sec. II. If the MPC algorithm includes the α and γ dispersion along with an EIS equivalent circuit, more information can be collected from the spectrum including the cell membrane behavior, the ion cloud around the membrane, and even certain molecules such as DNA, protein, and amino acid. Each of these EIS readings can be potentially a feedback signal to make a SACAPJ target a specific biomedical requirement. However, to achieve a higher frequency for the γ dispersion, another hardware should be considered to replace the impedance analyzer, which is discussed in Sec. IV.

IV. REAL-TIME PERMITTIVITY-IMPEDANCE MEASUREMENT FOR A HIGHER FREQUENCY RANGE

As introduced in Eq. (1), one can acquire real-time impedance based on the measurement of target permittivity. Unfortunately, commercially available impedance analyzers are usually unable to reach a frequency higher than 10 GHz. Therefore, an alternative setup is required to enable the EIS-based MPC for intracellular detection. One of the well-developed methods is using an open resonator of microwave usually works for a frequency above 30 GHz and even up to a couple of hundreds GHz, which is known as the Fabry–Pérot Resonator (FPR) introduced in Fig. 11. Therefore, for a detailed measurement of γ dispersion, the FPR can be an effective replacement of an impedance analyzer used in the EIS hardware. Typical hardware of the FPR includes a concave mirror on the top and a flat mirror below to perform as an open resonator. Two waveguides are located in the middle of the concave mirror and are connected to a Vector Network Analyzer (VNA). One of the waveguides feeds the Gaussian beam, which will then resonate between the mirrors and be collected by the other waveguide.[44–46]

The parameters measured in real-time by VNA can be S_{11} and S_{21}, which are two common concepts in two-port networks. S_{11} is the ratio of the power reflected by the system to the power input, while S_{21} is the ratio of the power transmitted through the system to the power input. To acquire the permittivity, we have to measure the resonance frequency from either S_{11} or S_{21} (both of them provide the same resonance frequency peaks) before and after placing the sample. Therefore, only one of them needs to be measured and in the following example, we show the permittivity results by measuring S_{11}.

An example of FPR measurement is shown in Fig. 12. Three pairs of S_{11} peaks can be found at around 94, 95, and 96 GHz in Fig. 12(a). For each pair, the existence of a sample shifts the peaks to the left with a distance depending on the frequency. The main equation to solve for permittivity is Eq. (15) numerically

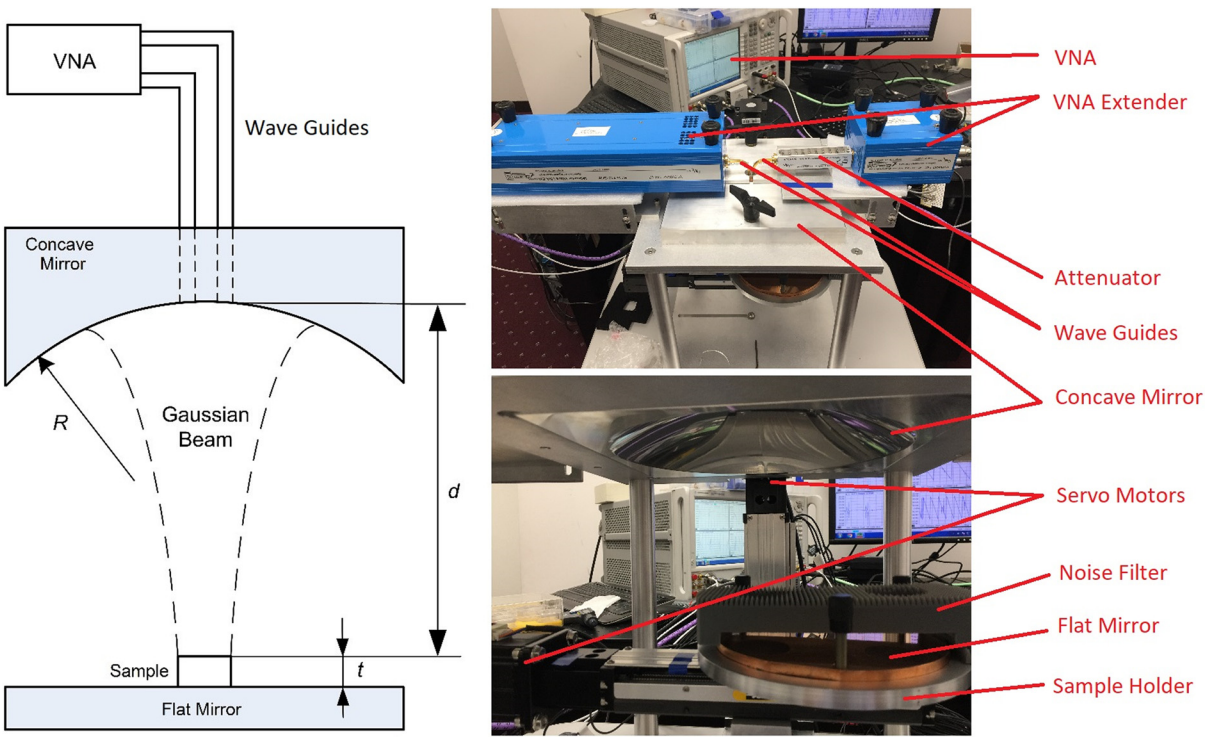

FIG. 11. A typical schematic of the Fabry–Pérot resonator for permittivity measurement and the hardware of the example experiment.

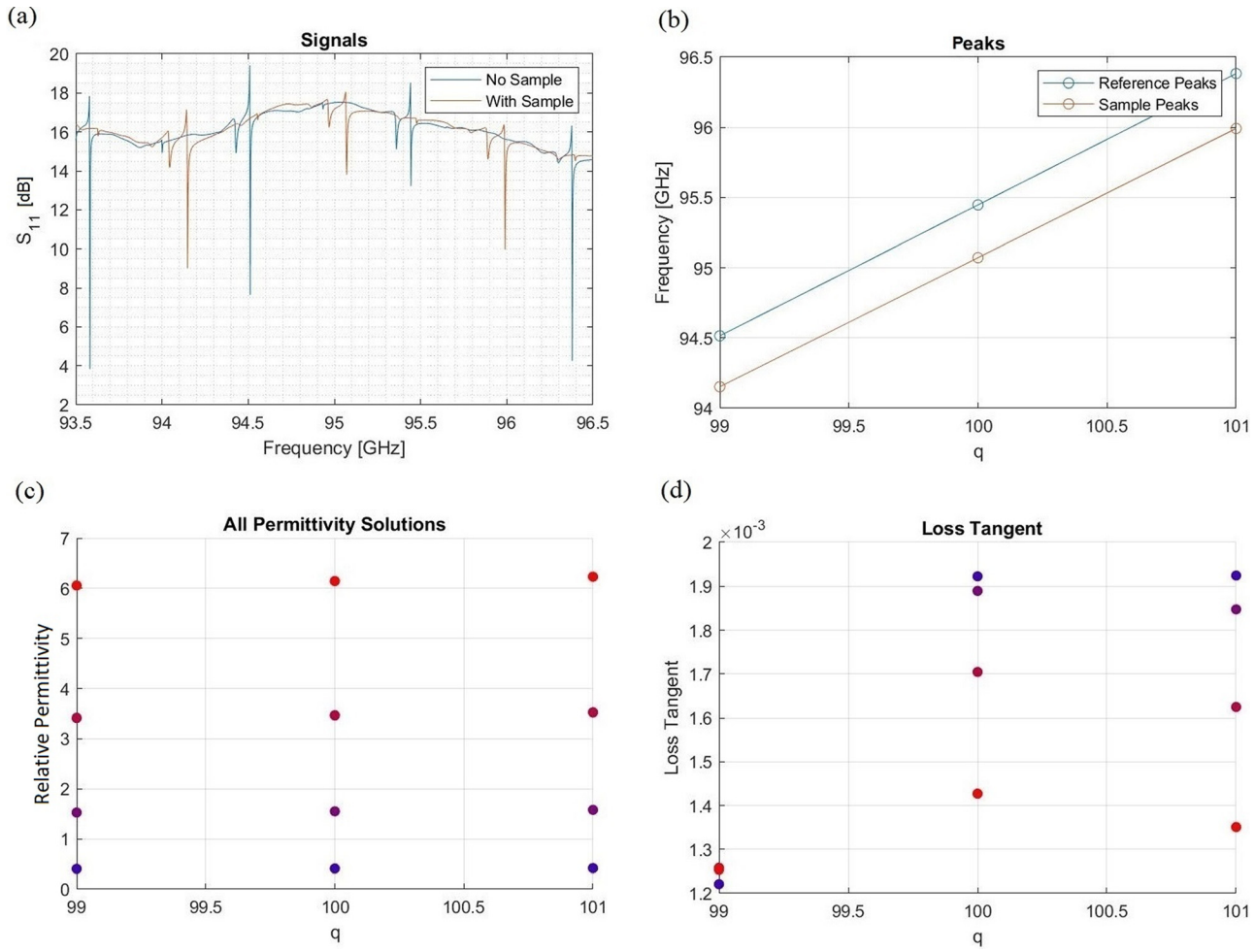

FIG. 12. An example of Fabry–Pérot resonator results. (a) The S_{11} signals of the open resonator; (b) the axial mode numbers; (c) the multiple solutions of sample permittivity; (d) the loss tangent values.

$$n^{-1}\tan\left[\mathrm{n}kt - \arctan\left(\frac{t}{nz_0}\right)\right] = -\tan\left[kd - \arctan\left(\frac{d+\frac{t}{\varepsilon_r}}{z_0}\right) - \arctan\left(\frac{t}{\varepsilon_r z_0}\right)\right], \quad (15)$$

where n is the refractive index that $n = \sqrt{\varepsilon_r}$, k is the wavenumber as a function of the resonance frequency f, and $z_0 = \sqrt{(d + t/\varepsilon_r)(R - d - t/\varepsilon_r)}$.[45,46] Other parameters in the equation such as t, d, and R are the geometry of the sample and resonator marked in Fig. 11. However, since the results are extremely sensitive to d and f, the user has to compute the exact d based on Eq. (16) rather than measure it,[45,46]

$$f = \frac{c}{2d}\left[q + 1 + \frac{2p + l + 1}{\pi}\arctan\left(\sqrt{\frac{d}{R-d}}\right)\right], \quad (16)$$

where p, l, and q are the TEM resonance mode that is denoted as $\mathrm{TEM}_{p,l,q}$. In this work, p and l are all zero. First, input the measured d and f from S_{11} when there is no sample to Eq. (16), this gives a q value. Since q has to be an integer, substituting the rounded q back to Eq. (16) will result in the exact d value. Figure 12(b) shows the mode number q for these resonance peaks. Finally, solving Eq. (15) with the exact d and f from S_{11} measured with the sample, multiple solutions of permittivity are acquired. In Fig. 12(c), four solutions for each peak are found from 0 to 7. The deviations of these solutions among peaks are limited, which indicates that the accuracy is reliable. However, to determine which permittivity value is for the real sample, either a measurement repeat with a different sample thickness or gross information of the permittivity range is required.

For any well-designed measurement techniques, the sample should not be altered by the measurement. In this case, the resonating microwave power applied to the sample should be low enough to avoid altering the sample. Although the VNA output power is not enough to heat the sample, computing the loss tangent for the system is a necessary double-check. The loss tangent is the tangent of dielectric loss angle in a complex plane. The real

part is the dielectric loss and the imaginary part is the ideal lossless term in one of the Maxwell equations considering the dielectric relaxation $\nabla \times \boldsymbol{H} = j\omega\varepsilon'\boldsymbol{E} + (\sigma - \omega\varepsilon'')\boldsymbol{E}$, where σ is the conductivity and $\boldsymbol{H}$ and $\boldsymbol{E}$ are the magnetic and electric field. Therefore, the loss tangent is a dimensionless ratio of the loss over lossless. For an FPR, the loss tangent values $\tan(\delta)$ are computed based on the equation[45,46]

$$\tan(\delta) = 2nkt(d + t\Delta)\left(Q_d^{-1} - Q_l^{-1}\right) \times \left\{2nkt\Delta - \Delta\sin\left[nkt - \arctan\left(\frac{t}{nz_0}\right)\right]\right\}^{-1}, \quad (17)$$

where Q_d is the quality factor with the sample placed. Also, $Q_l = Q_0\frac{2(t\Delta+d)}{D(\Delta+1)}$, where Q_0 is the quality factor of the resonator without a sample, and the equation

$$\Delta = n^2\left\{n^2\cos^2\left[nkt - \arctan\left(\frac{t}{nz_0}\right)\right] + \sin^2\left[nkt - \arctan\left(\frac{t}{nz_0}\right)\right]\right\}^{-1}, \quad (18)$$

provides the parameter Δ, in which, the quality factor of the microwave resonator can be found. Figure 12(d) shows the resulting loss tangents. Based on that, the power loss, in other words, the power absorbed by the sample can be thus computed as

$$P_{loss} = P_0 - P_0\exp(-\delta kt), \quad (19)$$

where δ is the tangent angle and P_{loss} and P_0 are the power absorbed by the sample and the power output from the VNA, respectively.

Overall, when applying the FPR on EIS, the cell-media target will be placed on the flat mirror in the FPR. The real-time permittivity can be measured, and the impedance can thus be computed using Eq. (1).

In addition to the typical design of FPR shown above, some variations can also be considered for the EIS-SACAPJ setup. One example is the Gaussian beam scanning array (GBSA), which is an electronic beam scanning device able to sweep the beam over the cell-culture dish for *in vitro* works and tissues for clinical applications. The GBSA is similar to the military-use radar such as the active electronically scanned array (AESA) widely used on naval vessels and jet fighters in the present days. Therefore, the advantage of GBSA is to sweep the target in real-time with spatial resolution, such as the wells in a cell culture plate. As shown in Fig. 13, in the GBSA setup, the feeding waveguide array is fixed on the left while the receiving one locates on the right, while the Gaussian beam can still be reflected on the flat mirror in the middle and holding the sample.

The feed waveguide array includes multiple waveguide emitters, and each of them emits the beam with a phase shift. A main bright fringe of the resulting interfered beams can thus be manipulated by the phase shift. As shown in Fig. 14, a flat mirror is located at the bottom $x = 0$ to reflect the Gaussian beam emitted from an antenna array including five emitters in a row with a 1 mm gap between. Each emitter emits a Gaussian beam based on the following equations:[47]

$$E(x,z) = \frac{W_0}{W_B}\exp\left[-\frac{(x-x_0)^2}{W_B^2} - \frac{j\pi z}{\lambda} - \frac{j\pi(x-x_0)^2}{\lambda R_B} + j\varphi\right], \quad (20)$$

$$\varphi = \arctan\left(\frac{\lambda z}{\pi W_0^2}\right) + \Delta\varphi, \quad (21)$$

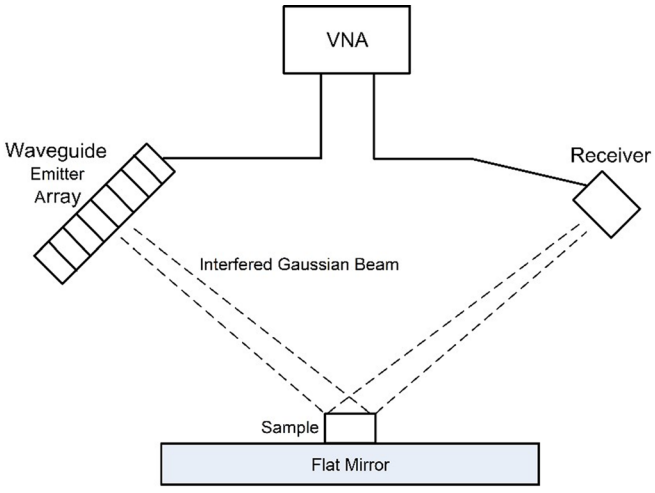

FIG. 13. A typical setup of a Gaussian beam scanning array.

$$W_B = W_0\sqrt{1 + \left(\frac{\lambda z}{\pi W_0^2}\right)^2}, \quad (22)$$

$$R_B = z + \frac{\pi^2 W_0^4}{z\lambda^2}, \quad (23)$$

where W_B is the beam radius, R_B is the beam wavefront curvature radius, λ is the wavelength, φ is the phase with the first term at the right-hand side representing the Gouy phase, $\Delta\varphi$ is the phase difference between emitters, W_0 is the beam waist radius at the emitter location, x_0 is the emitter location, and x and z are the coordinates. The Gaussian beams shown in Fig. 14 are setup at 200 GHz with a 10 dB gain and $W_0 = 3$ mm. From Figs. 14(a)–14(e), all five emitters emit Gaussian beams toward the flat mirror at the same angle but with a phase shift of -0.1125π. The resulting interfered electric field is depicted in Fig. 14(f) that a bright fringe hits on the mirror at around $z = 0.09$ m and reflected by the mirror. From Figs. 14(g)–14(l), the phase difference is varied from -0.075π to 0.1125π, and the resulting reflection point also moves to 0.12 m. Figure 14 indicates that the interfered beam can sweep over a centimeter-scale sample by manipulating the phase difference as expected.

Therefore, in the EIS-biomedical applications, the cell-media target can be placed on the flat mirror, and the GBSA setups can sweep the beam over the plate and measure the impedance in each well. Note that the beam width is proportional to the wavelength. To achieve an impedance spectrum at a lower frequency but keeping the spatial resolution, concave mirrors can be used to focus the beam as an intermediate stage between the emitter array and the sample. Overall, the advantage of GBSA variation of FPR compared with the vertical setup is obvious, that a GBSA scans an area of cell-culture dish or tissue with spatial resolution in an instant while the traditional FPR setup requires mechanical structures to move the sample.

V. CONCLUSIONS

In this work, we summarized the future potential of replacing the MTT test with EIS real-time measurement in the MPC method to achieve a SACAPJ optimization. Rather than collecting the parameters

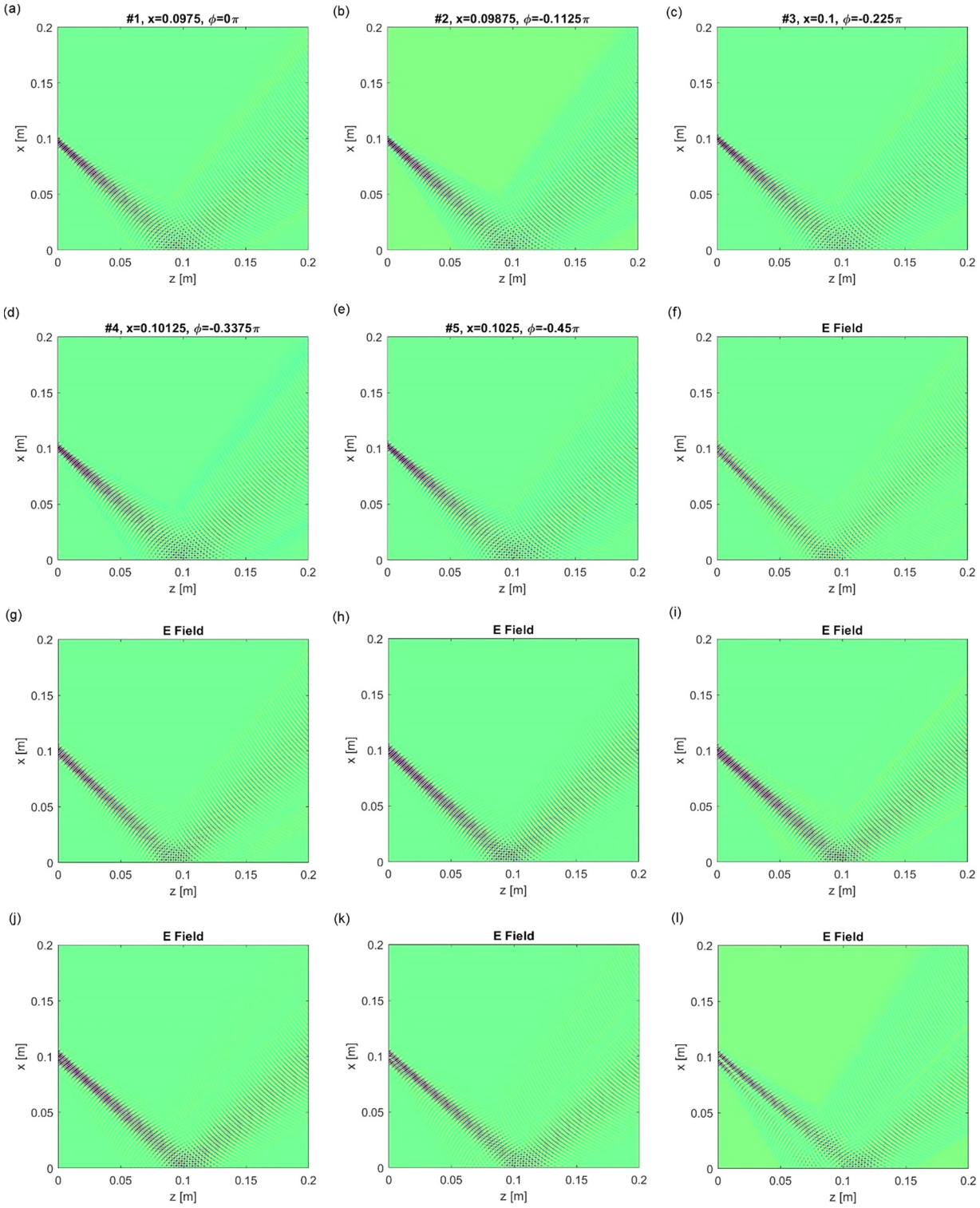

FIG. 14. Manipulating the bright fringe of five interfering Gaussian beams. (a)–(e) The electric field of each antenna is located at $z = 0$ with a 1 mm gap between and a phase difference of -0.1125π; (f) the resulting interfered beam; (g)–(l) the resulting interfered beams with the same geometry but the phase difference are -0.075π, -0.0375π, 0, 0.0375π, 0.075π, and 0.1125π accordingly.

of plasma jet and non-biomedical targets as feedback signals,[21,48] we correlate the EIS signal in the β dispersion range with cell viability directly as a feedback signal. In the example of treating U87MG, a lower impedance at 549 MHz represented lower cell viability, and it had been proved that such impedance decrement can be manipulated by the applied voltage in a control loop. Also, we discussed a more advanced MPLC method based on GP as an upgrade version of the previous MPC. As an example, the simulation shows a successful approach of the cell viability from the no-control case to the ideal response. Therefore, the potential to achieve a periodic SACAPJ control by using the learning based MPC algorithm coupling with EIS is revealed.

Moreover, we also discussed the possibility of using the equivalent circuit, α and γ dispersion in the EIS measurement to make the SACAPJ targeting the cell membrane behavior, molecules in the bulk media for an *in vitro* experiment, and even an acoustic wave in a cell, which can explain the cell activation process. To reach such a high-frequency measurement, we suggest replacing the impedance analyzer with FPR and even GBSA to achieve a real-time quick scan for cell culture plates with a spatial resolution for wells. A real model of FPR has been tested and proved that the FPR works for measuring permittivity and impedance. A 2D GBSA model with beam reflection is also tested in simulation. An actual model of it will be built as the next step of this work. Both the FPR and the electronically scanning array are well-developed technology. Therefore, the combination of this hardware for an actual adaptive plasma cancer treatment can be expected in the near future.

ACKNOWLEDGMENTS

This work was supported by the National Science Foundation (Grant No. 1747760).

DATA AVAILABILITY

The data that support the findings of this study are available from the corresponding author upon reasonable request.

REFERENCES

[1]G. Fridman, G. Friedman, A. Gutsol, A. B. Shekhter, V. N. Vasilets, and A. Fridman, Plasma Process. Polym. **5**, 503 (2008).
[2]G. Fridman, M. Peddinghaus, M. Balasubramanian, H. Ayan, A. Fridman, A. Gutsol, and A. Brooks, Plasma Chemistry and Plasma Processing **26**, 425 (2006).
[3]M. Laroussi, IEEE Trans. Plasma Sci. **24**, 1188 (1996).
[4]M. Keidar, Plasma Sources Sci. Technol. **24**, 033001 (2015).
[5]M. Keidar, D. Yan, and J. H. Sherman, *Cold Plasma Cancer Therapy* (Morgan & Claypool Publishers, 2019).
[6]M. Keidar and I. Beilis, *Plasma Engineering: Applications from Aerospace to Bio and Nanotechnology* (Academic Press, 2013).
[7]A. Fridman, A. Alexander, A. Lawrence, F. Routledge, L. A. Kennedy, and P. Square, *Plasma Physics and Engineering* (CRC Press, 2004).
[8]M. Keidar, R. Walk, A. Shashurin, P. Srinivasan, A. Sandler, S. Dasgupta, R. Ravi, R. Guerrero-Preston, and B. Trink, Br. J. Cancer **105**, 1295 (2011).
[9]M. Keidar, A. Shashurin, O. Volotskova, M. A. Stepp, P. Srinivasan, A. Sandler, and B. Trink, Phys. Plasmas **20**, 057101 (2013).
[10]L. Lin, Y. Lyu, B. Trink, J. Canady, and M. Keidar, J. Appl. Phys. **125**, 153301 (2019).
[11]L. Lin, D. Yan, E. Gjika, J. H. Sherman, and M. Keidar, ACS Appl. Mater. Interfaces **11**, 30621 (2019).
[12]S. A. Norberg, E. Johnsen, and M. J. Kushner, J. Appl. Phys. **118**, 013301 (2015).
[13]N. Mericam-Bourdet, M. Laroussi, A. Begum, and E. Karakas, J. Phys. D **42**, 055207 (2009).
[14]L. Lin and M. Keidar, Phys. Plasmas **23**, 083529 (2016).
[15]G. Uchida, A. Nakajima, T. Ito, K. Takenaka, T. Kawasaki, K. Koga, M. Shiratani, and Y. Setsuhara, J. Appl. Phys. **120**, 203302 (2016).
[16]D. Breden and L. L. Raja, Plasma Sources Sci. Technol. **23**, 065020 (2014).
[17]M. Keidar, D. Yan, I. I. Beilis, B. Trink, and J. H. Sherman, Trends Biotechnol. **36**, 586 (2018).
[18]E. Gjika, S. Pal-Ghosh, A. Tang, M. Kirshner, G. Tadvalkar, J. Canady, M. A. Stepp, and M. Keidar, ACS Appl. Mater. Interfaces **10**, 9269 (2018).
[19]E. Gjika, S. Pal-Ghosh, L. Lin, G. Tadvalkar, Z. Chen, C. Yoing, J. Canady, J. Sherman, M. A. Stepp, and M. Keidar, Clin. Plasma Med. **9**, 16 (2018).
[20]Y. Lyu, L. Lin, E. Gjika, T. Lee, and M. Keidar, J. Phys. D **52**, 185202 (2019).
[21]A. Mesbah and D. B. Graves, J. Phys. D **52**, 30LT02 (2019).
[22]M. Witman, D. Gidon, D. B. Graves, B. Smit, and A. Mesbah, Plasma Sources Sci. Technol. **28**, 095019 (2019).
[23]H. Schättler and U. Ledzewicz, *Optimal Control for Mathematical Models of Cancer Therapies* (Springer, Berlin, 2015).
[24]E. T. Whittaker, *A History of the Theories of Aether and Electricity from the Age of Descartes to the Close of the Nineteenth Century* (Longmans, Green and Company, 1910).
[25]A. Thomasset, Lyon Med. **28**, 107 (1962).
[26]H. P. Schwan and C. F. Kay, Circ. Res. **4**, 664 (1956).
[27]H. P. Schwan and C. F. Kay, Ann. N. Y. Acad. Sci. **65**, 1007 (1957).
[28]H. P. Schwan and G. M. Pierson, Am. J. Phys. Med. **33**, 371 (1954).
[29]H. P. Schwan and G. M. Pierson, Am. J. Phys. Med. **34**, 425 (1955).
[30]U. G. Kyle, I. Bosaeus, A. D. De Lorenzo, P. Deurenberg, M. Elia, J. M. Gómez, B. L. Heitmann, L. Kent-Smith, J.-C. Melchior, M. Pirlich, H. Scharfetter, A. M. W. J. Schols, and C. Pichard, Clin. Nutr. **23**, 1430 (2004).
[31]I. O. K. Owino and O. A. Sadik, Electroanalysis **17**, 2101 (2005).
[32]R. Ehret, W. Baumann, M. Brischwein, A. Schwinde, B. Wolf, and K. Stegbauer, Biosens. Bioelectron. **12**, 29 (1997).
[33]V. F. Lvovich, *Impedance Spectroscopy Applications to Electrochemical and Dielectric Phenomena* (John Wiley & Sons, New Jersey, 2012).
[34]M. E. Orazem and B. Tribollet, *Electrochemical Impedance Spectroscopy* (John Wiley & Sons, New Jersey, 2008).
[35]A. J. Brad and L. R. Faulkner, *Electrochemical Methods Fundamentals and Applications* (John Wiley & Sons, New York, 1980).
[36]V. F. Lvovich and M. F. Smiechowski, Electrochim. Acta **53**, 7375 (2008).
[37]H. P. Schwan, Adv. Biol. Med. Phys. **5**, 147 (1957).
[38]D. Yan, W. Xu, X. Yao, L. Lin, J. H. Sherman, and M. Keidar, Sci. Rep. **8**, 15418 (2018).
[39]D. Yan, L. Lin, W. Xu, and N. Nourmohammadi, J. Phys. D **52**, 445202 (2019).
[40]N. N. Kositsky, A. I. Nizhelska, and G. V. Ponezha, No Place to Hide **3**, 1 (2001).
[41]V. M. Kontorovich and A. M. Glutsyuk, Sov. Phys. JETP **14**, 852 (1962).
[42]J. Xu, X. Jiang, N. Fang, E. Georget, and R. Abdeddaim, Sci. Rep. **5**, 10678 (2015).
[43]K. Williams and C. Rasmussen, *Gaussian Processes for Machine Learning* (MIT Press, Cambridge, MA, 2006).
[44]A. L. Cullen and P. K. Yu, Proc. R. Soc. London Ser. A **325**, 493 (1971).
[45]T. M. Hirvonen, P. Vainikainen, A. Lozowski, A. V. Raisanen, and B. L. Tangent, IEEE Trans. Instrum. Meas. **45**, 780 (1996).
[46]J. J. Choi and W. B. Seo, Int. J. Infrared Millimeter Waves **22**, 1837 (2001).
[47]R. Paschotta, "Article on Gaussian beams," *Encyclopedia of Laser Physics and Technology* (Wiley-VCH, 2008).
[48]D. Gidon, X. Pei, A. D. Bonzanini, D. B. Graves, A. Mesbah, and S. Member, IEEE Trans. Radiat. Plasma Med. Sci. **3**, 597 (2019).